POLITECNICO DI TORINO
Repository ISTITUZIONALE

Microseismicity of an Unstable Rock Mass: From Field Monitoring to Laboratory Testing

Original
Microseismicity of an Unstable Rock Mass: From Field Monitoring to Laboratory Testing / Colombero, C., Comina, C., Vinciguerra, S., Benson, P.M.. - In: JOURNAL OF GEOPHYSICAL RESEARCH. SOLID EARTH. - ISSN 2169-9313. - 123:2(2018), pp. 1673-1693. [10.1002/2017JB014612]

Availability:
This version is available at: 11583/2707668 since: 2018-05-18T15:46:34Z

Publisher:
Blackwell Publishing Ltd

Published
DOI:10.1002/2017JB014612

Terms of use:

This article is made available under terms and conditions as specified in the corresponding bibliographic description in the repository

Publisher copyright

(Article begins on next page)

29 November 2026

AGU PUBLICATIONS

JGR

Journal of Geophysical Research: Solid Earth

RESEARCH ARTICLE
10.1002/2017JB014612

Special Section:
Seismic and micro-seismic signature of fluids in rocks: Bridging the scale gap

Microseismicity of an Unstable Rock Mass: From Field Monitoring to Laboratory Testing

C. Colombero[1], C. Comina[1], S. Vinciguerra[1], and P. M. Benson[2]

[1]Dipartimento di Scienze della Terra, Università degli Studi di Torino, Turin, Italy, [2]Rock Mechanics Laboratory, School of Earth an Environmental Sciences, University of Portsmouth, Portsmouth, UK

Abstract The field-scale microseismic (MS) activity of an unstable rock mass is known to be an important tool to assess damage and cracking processes eventually leading to macroscopic failures. However, MS-event rates alone may not be enough for a complete understanding of the trigger mechanisms of mechanical instabilities. Acoustic Emission (AE) techniques at the laboratory scale can be used to provide complementary information. In this study, we report a MS/AE comparison to assess the stability of a granitic rock mass in the northwestern Italian Alps (Madonna del Sasso). An attempt to bridge the gap between the two different scales of observation, and the different site and laboratory conditions, is undertaken to gain insights on the rock mass behavior as a function of external governing factors. Time- and frequency-domain parameters of the MS/AE waveforms are compared and discussed with this aim. At the field scale, special attention is devoted to the correlation of the MS-event rate with meteorological parameters (air temperature and rainfalls). At the laboratory scale, AE rates, waveforms, and spectral content, recorded under controlled temperature and fluid conditions, are analyzed in order to better constrain the physical mechanisms responsible for the observed field patterns. The factors potentially governing the mechanical instability at the site were retrieved from the integration of the results. Abrupt thermal variations were identified as the main cause of the site microsesimicity, without highlighting irreversible acceleration in the MS-event rate potentially anticipating the rock mass collapse.

Key Points:
- The microseismicity of an unstable cliff is studied using spectral analysis, source location, and event-rate correlation with external factors
- AE laboratory tests are performed to reproduce the site microseismicity under controlled fluid and temperature conditions
- Thermal stresses are found to be the main cause inducing microcracking processes at both the field and laboratory scale

Correspondence to:
C. Colombero,
chiara.colombero@unito.it

Citation:
Colombero, C., Comina, C., Vinciguerra, S., & Benson, P. M. (2018). Microseismicity of an unstable rock mass: From field monitoring to laboratory testing. *Journal of Geophysical Research: Solid Earth*, *123*. https://doi.org/10.1002/2017JB014612

Received 27 JUN 2017
Accepted 30 JAN 2018
Accepted article online 6 FEB 2018

©2018. American Geophysical Union. All Rights Reserved.

1. Introduction

The microseismic activity of an unstable rock mass represents a useful tool to assess damage and early-stage cracking processes that may eventually lead to macroscopic failures. The analysis of the fracture-related microseismic (MS) events, in terms of temporal rate and source locations, can provide useful information on the acceleration to failure and on the identification of the most prone-to-fail compartments and slip surfaces. However, MS events alone may not be enough for a complete understanding of the factors governing mechanical instabilities, particularly in complex field environments, where it is difficult to directly link external stimuli to environmental considerations. For a more complete comprehension, field analyses can be complemented with acoustic emission (AE) experiments at the laboratory scale. Laboratory tests have the advantage of controlled boundary conditions (e.g., water content and temperature). Since the early 1970s, there has been an increasing interest in the use of AE/MS techniques for field and laboratory investigations of geological materials and engineering applications. These studies apply to different scales and investigation environments, using a different frequency range of the monitoring devices (Hardy, 2003), varying from 1–100 Hz (MS) to the kHz-to-MHz range (AE).

In the last 20 years, MS systems have been extensively deployed on a variety of rock mass settings, ranging from preeruptive volcanic edifices and lahars (e.g., Diodati et al., 1991; Gambino et al., 2004) to debris flows and ice avalanches (e.g., Caplan-Auerbach & Huggel, 2007) and mining environments (e.g., Young & Collins, 2001). Dealing with rock-slope stability, Amitrano et al. (2005) and Senfaute et al. (2009) examined the microseismic signals recorded prior to the collapse of a 2,000 m^3 coastal cliff sector located at Mesnil-Val (Normandie, France), demonstrating that MS events can provide information about the incipient failure of internal rock bridges. After this study, applications of the method expanded to several test sites, especially in the Alpine context. These studies led to large data sets of recorded events (e.g., in Amitrano et al., 2010; Helmstetter & Garambois, 2010; Lévy et al., 2011; Spillmann et al., 2007; Walter & Joswig, 2009), with challenging classification and location tasks due to strong signal scattering and attenuation caused by the heterogeneous seismic velocity field of the unstable slopes. Consequently, a large part of these studies were mainly focused on the search for seismic precursors before slope failure and on the relation between

seismic events (ruptures and rockfalls), displacement-rate measurements, and external governing factors (particularly, climatic parameters).

Numerous external factors can promote slope instabilities. The most widespread factors include excessive rainfall and the consequent modification of the hydrogeological parameters of the unstable bodies, freeze-thaw cycles and snow melting, temperature variations, earthquake shaking, volcanic activity, and human action (Gariano & Guzzetti, 2016). Although these triggering causes are globally accepted, their influence on possible instabilities are strongly dependent on the nature of the unstable body and on the site location (elevation, exposure, and climate). Depending on the environmental factors, the influence of one or some of these parameters may therefore dominate on the others. For example, rockslides and rockfalls located in high mountainous areas (hard rocks and freezing climate) are mostly driven by temperature variations (Paranunzio et al., 2015). However, although individual mechanisms of physical weathering have been addressed through field studies (e.g., Eppes et al., 2010; McFadden et al., 2005), numerical modeling (e.g., Moores et al., 2008), and laboratory experiments (e.g., McKay et al., 2009; Molaro & McKay, 2010), few studies have been able to demonstrate an unequivocal correlation between environmental factors and rock cracking. Besides rapid thermal variations, there are a large number of cyclic processes acting on rock masses, which constitute physical weathering agents (Eppes et al., 2010; McFadden et al., 2005; McKay et al., 2009; Moores et al., 2008). These include daily and seasonal cycles and other short-term heating-cooling cycles (effect of wind), wetting-drying cycles, and freeze-thaw cycles. Gunzburger et al. (2005) demonstrated that daily thermal cycles are able to induce shearing along existing fractures, particularly when temporal or spatial temperature gradients are the highest. Since an increase in moisture reduces the tensile strength and fatigue limit of the rock (Burdine, 1963), the combined effect of moisture and temperature is likely to enhance thermal expansion and contraction processes (Halsey, 1996; Yatsu, 1988). Since microseismicity has proven to be a valuable tool to infer incipient fracture processes, correlations between MS-event rates and meteorological driving factors have often been attempted. In particular, the Séchilienne landslide (French Alps) exhibited clusters of microseismicity that were weakly but nonetheless correlated with rainfall (Helmstetter & Garambois, 2010). Although rockfalls occurred on a regular basis with respect to the instance of precipitation, a strong variation in the numbers of rockfalls per day was noted even for the same rainfall intensity, making a trigger threshold impossible to establish. From the combined analysis of rainfall and temperature data, Lévy et al. (2010) found that an increase in the microseismicity of an unstable rock column could be correlated with probable freeze-thaw cycles. Due to the environmental conditions common to the Matterhorn Peak (3,829 m above sea level), Amitrano et al. (2010) used air temperature to investigate possible relations with the microseismicity linked to slope deformation. Clusters of MS events occurred in specific days characterized by abrupt negative or positive temperature changes. Amitrano et al. (2012) and Girard et al. (2013) further demonstrated thermal and freezing-induced stresses as crucial microfracturing causes in high-altitude rock faces, by means of on-site AE monitoring. Conversely, Spillmann et al. (2007) did not find either obvious seasonal variations or correlations between temperature/rainfalls and microseismicity recorded at the Randa gneissic rockslide (Swiss Alps). Importantly, in all of these studies, air temperature and rainfall trends are the only external parameters that have been tentatively correlated to the microseismic activity in unstable sites.

Experiments at an intermediate scale between field and laboratory were conducted in an attempt to clarify the role of external factor on fracture-related microseismicity (Garbini, 2009; Swami, 2011; Warren et al., 2013). Here long-term multisensor studies of acoustic emissions on small-size granitic boulders exposed to ambient conditions were conducted. The surface of each natural block was instrumented with AE sensors, strain gauges, thermocouples, and a surface moisture sensor. During a 6-month monitoring campaign, AE events were typically observed to cluster during late afternoon and evening hours and related to sudden drops or rises of surface temperature. These negative/positive thermal variations were directly correlated to surface strain variations, indicating contraction/expansion of the boulder. While the highest number of AE events occurred when the rock was wet, a significant number of events was still detected in dry conditions. Even when AE events occurred during precipitations, AE events often preceded the rainfall occurrence.

In this study, we present a microseismicity study of an unstable granitic cliff located in northwestern Italian Alps (Madonna del Sasso, VB), combined with laboratory rock physics experiments, to better understand the gap in observation scale. At the field scale, particular attention is devoted to search for correlations

between the long-term MS-event rate and the meteorological parameters (rainfall and temperature). On this basis, appropriate AE laboratory tests have been developed for qualitative comparison. This makes use of both AE rate and spectral content as a function of controlled temperature and fluid conditions, so as to constrain the physical mechanisms responsible for the observed field patterns. Such laboratory tests, integrating conventional triaxial apparatus with AE recordings, have already been proven to give experimental insights to fracture nucleation, growth, and coalescence into major fractures and in the underlying micromechanisms (Lockner et al., 1991). These studies always referred to investigation targets located at considerable depths, varying from tunneling applications to volcanic systems and earthquake dynamics (Browning et al., 2016). The adopted laboratory instrumentations and loading conditions were therefore justified by the site stress fields. Semiquantitative AE/MS comparisons could consequently be established considering similarities between laboratory and field waveforms (e.g., amplitude and duration) or related spectral contents (i.e., similarities in the spectrograms), in order to characterize the mechanism controlling the frequency distribution (e.g., Benson et al., 2008, 2010; Burlini et al., 2007; Fazio et al., 2017). However, the present study has to face different near-surface site conditions imposed by an outcropping fractured cliff. The adopted laboratory procedure was therefore chosen as a compromise between the available testing instrumentation and the need of studying the influence of temperature and fluids on fractured samples, in order to obtain a proxy for the factors controlling the microseismicity of the site.

2. Microseismicity at the Field Scale

2.1. Test Site and Monitoring Network

In October 2013, a microseismic monitoring network was installed in the surroundings of the XIII-century church of Madonna del Sasso, in northwestern Italian Alps (Figure 1a). The site is located on the western shore of the Orta Lake, at the top of a steep homogeneous granitic cliff (*Granito di Alzo*), delimited by subvertical faces on the north, south, and east sides (Figure 1b). The cliff lies close to the NE edge of the SW-NE elongated Alzo-Roccapietra Pluton, which is delimited by three main faults: the Pogallo Line, to the west, the Cossato-Mergozzo-Brissago Line, to the east, and the Cremosina Line, to the south (Boriani et al., 1990; Boriani & Giobbi, 2004).

Near the summit of the cliff, two potentially unstable blocks are partially isolated from the stable rock mass by the presence of four main deep and open fractures (K1 to K4, in Figures 1c and 1d). In particular, the first block "A" is limited on the vertical sides by fractures K2, K1, and K4 at the northern edge of the cliff. The second southern block "B" is cut by fractures K2 and K4. Both A and B are truncated at the base by K3 (Figures 1c and 1d). Fracture orientations partially reflect the orientations of the main tectonic lineaments of the area. Regional stresses could have therefore contributed to fracture formation, but since no recent tectonic activity is highlighted on these regional faults, the present fracture dynamic is expected to be mainly driven by gravity and external weathering factors.

Displacements, localized collapses in the yard at the top of the cliff and progressive fracture opening with associated intense air upflows, have been observed and measured on site since 1981. Given the almost inaccessible steep morphology of the cliff, a preliminary complete characterization of the 3-D fracture setting was achieved from the combination of field observations, noncontact measurements of fracture orientations, active and passive seismic surveys (Colombero et al., 2016, 2017). In addition, it was demonstrated from noise spatial directivity and numerical modeling that the cliff vibration directions are mainly controlled by the orientations of fracture K2 and K4. These fractures have indeed the largest opening (~0.5 m) and persistence within the rock mass (~15 m, from Colombero et al., 2017). In addition, past displacement monitoring campaigns at the site (crackmeters on fractures K1 and K2 in 1991–1992 and wire extensometers across fracture K4 in 2008–2009) highlighted a partially reversible seasonal fluctuation of fracture opening, driven by air temperature fluctuations (Regione, 1993). Maximum fracture opening was recorded during winter months, likely due to the rock mass thermal contraction, while minimum opening was found in summer as a result of the rock mass thermal expansion. In addition, the maximum openings were recorded at the top of the cliff (3 mm/yr, with residual displacement of approximately 2 mm/yr) while measurements at lower altitudes across the same fractures showed lower displacement rates (1.3 mm/yr, with no residual displacement), suggesting a foot control on the block displacements (Colombero et al., 2016).

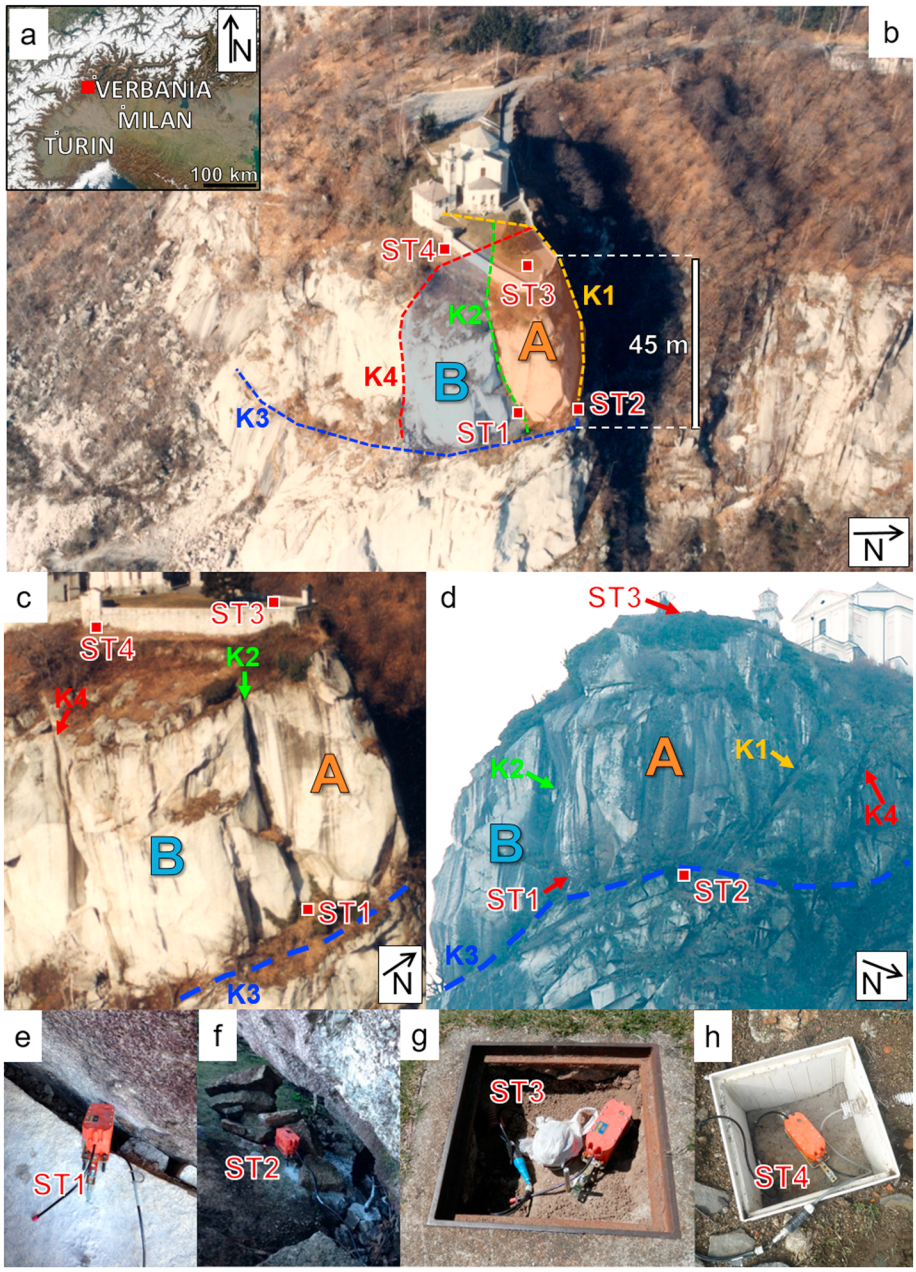

Figure 1. (a) Geographical location of the test site (Madonna del Sasso), in northwestern Italian Alps. (b) Eastern, (c) Southern, and (d) Northern aerial views of the site with indication of fracture traces (K1 to K4) and location of the microseismic stations (ST1 to ST4). The two unstable blocks are highlighted by letters A and B. Detail on the microseismic monitoring stations: (e) ST1, (f) ST2, (g) ST3, and (h) ST4.

In accordance with past monitoring studies, the microseismic network was designed to specifically monitor the unstable block A, with four seismic stations (4.5 Hz triaxial geophones). Two stations were located near the foot of the unstable block, on the southeast (ST1, Figure 1e) and north (ST2, Figure 1f) faces of the cliff, while the other two stations were located in shallow manholes at the cliff summit, respectively, at the top of block A (ST3, Figure 1g) and outside the fractured sector (ST4, Figure 1h). The latter was consequently used as a reference station. Each station was fixed on a steel support (Figures 1e–1h) and anchored (for approximately 5 cm) in the granitic bedrock (ST1 and ST2) or in the basal concrete slab of the shallow manholes (for ST3 and ST4). The four stations were connected to an acquisition system (12-channel "Granite," Kinemetrics Inc.) located a few meters to the east of ST4. The system was completed by a Global Positioning System antenna, for timing and synchronization of the acquired seismic traces. Power supply

was provided by direct connection to the electric line of the site. Wireless data transmission was set to enable remote system control and data download. Short-duration seismic events were recorded at 1 kHz sampling frequency, using a STA/LTA (Short-Time Average over Long-Time Average) detection algorithm (STA window = 0.3 s, LTA window = 30 s, and STA/LTA trigger threshold = 6). The total number of hits (the number of times in which a channel exceeds the STA/LTA threshold) to trigger the system was set to 12, excluding contributions coming from the upper stations (ST3 and ST4), in order to reduce the recording of anthropic disturbances linked to human presence and activities on the site. Due to a breakdown of the acquisition system between August 2014 and May 2015, MS events were recorded in two main time windows: the first between October 2013 and August 2014, and the second between May 2015 and February 2016. In the monitored time windows, more than 12,600 seismic events were recorded, including MS events likely to be related to fracture processes within the rock mass.

2.2. MS Processing Methods

Classification of the recorded data set was performed integrating both visual analysis of the event spectrograms (Helmstetter & Garambois, 2010) and cluster analysis of reference parameters, including signal maximum amplitude, frequency peak in the Fourier spectrum, kurtosis, and duration.

The location of the extracted MS events was then carried out using the nonlinear probabilistic approach of Lomax et al. (2000). To improve location results, a 3-D velocity model of the cliff was on-purpose built, combining a laser-scanning Digital Terrain Model with the results of seismic surveying at the site (from Colombero et al., 2016). This model was calibrated and tested by relocation of georeferenced hammer strokes performed at the cliff summit. The final 3-D model velocities vary from 300 m/s (in air, outside the rock mass) to 3,200 m/s (in deep intact granite). Gaussian distribution functions were used in the nonlinear probabilistic approach to represent 4 ms uncertainty in the reading of first arrival times (up to 10 m of spatial uncertainty considering the average velocity of the 3-D model = 2,400 m/s) and 0.5 ms uncertainty in the theoretical travel times (corresponding to 1.2 m of uncertainty considering the 3-D model average velocity). For each located MS event, the maximum likelihood point of the complete nonlinear location Probability Density Function (PDF) was finally selected as the optimal hypocenter. Due to the nonlinearity of the problem, the PDFs completely describing the location results are not ellipsoidal and in some cases are somewhat irregular. Nevertheless, traditional Gaussian estimators and related confidence ellipsoids are still useful indicators of uncertainties in the location, especially when the complete nonlinear PDFs are more regular and less scattered. As a consequence, confidence ellipsoids were retrieved as well in addition to the maximum likelihood solutions, to evaluate the uncertainties in the location results.

Particular attention was finally devoted to investigate the temporal correlations and effects of temperature fluctuations and rainfalls on the MS-event rate.

2.3. MS Results: Spectrograms and Source Location

From the original data set, 1,773 impulsive and short-duration signals with a triangular envelope and clear coda (Figure 2) were recognized as possible MS events originating from microcracking processes. This hypothesis is supported by spectral data that show a recurrent clear high-frequency emerging onset followed by a sudden exponential decay of the high-frequency content with time, in approximately the 75% of the events (Figures 2a and 2b). In the remaining 25% of the events, the high-frequency content ($>$ 30 Hz) is partially or totally missing (Figures 2c and 2d). MS events were seen to occur either as single events or in sequences of more events at different time spacing (Figures 2e and 2f). All MS events showed variable amplitude, high kurtosis values, and frequency peaks usually centered around 20 Hz.

These time- and frequency-domain peculiarities of the detected MS events are in agreement with those reported by several authors for MS events recorded on other unstable sites (e.g., Helmstetter & Garambois, 2010; Lévy et al., 2010). At the laboratory scale, similar spectral shapes have been identified in relation to rock-sample fracturing or slip processes on preexisting surfaces (e.g., Burlini et al., 2007; Benson et al., 2008, 2010).

Approximately 45% of the detected MS events were recorded only by ST1 and/or ST2. The absence of related recordings on the upper stations ST3 and ST4 suggested interpreting these signals as low-energy events occurring close to the foot of the unstable volume. Frequently (30% of the data set), all the three

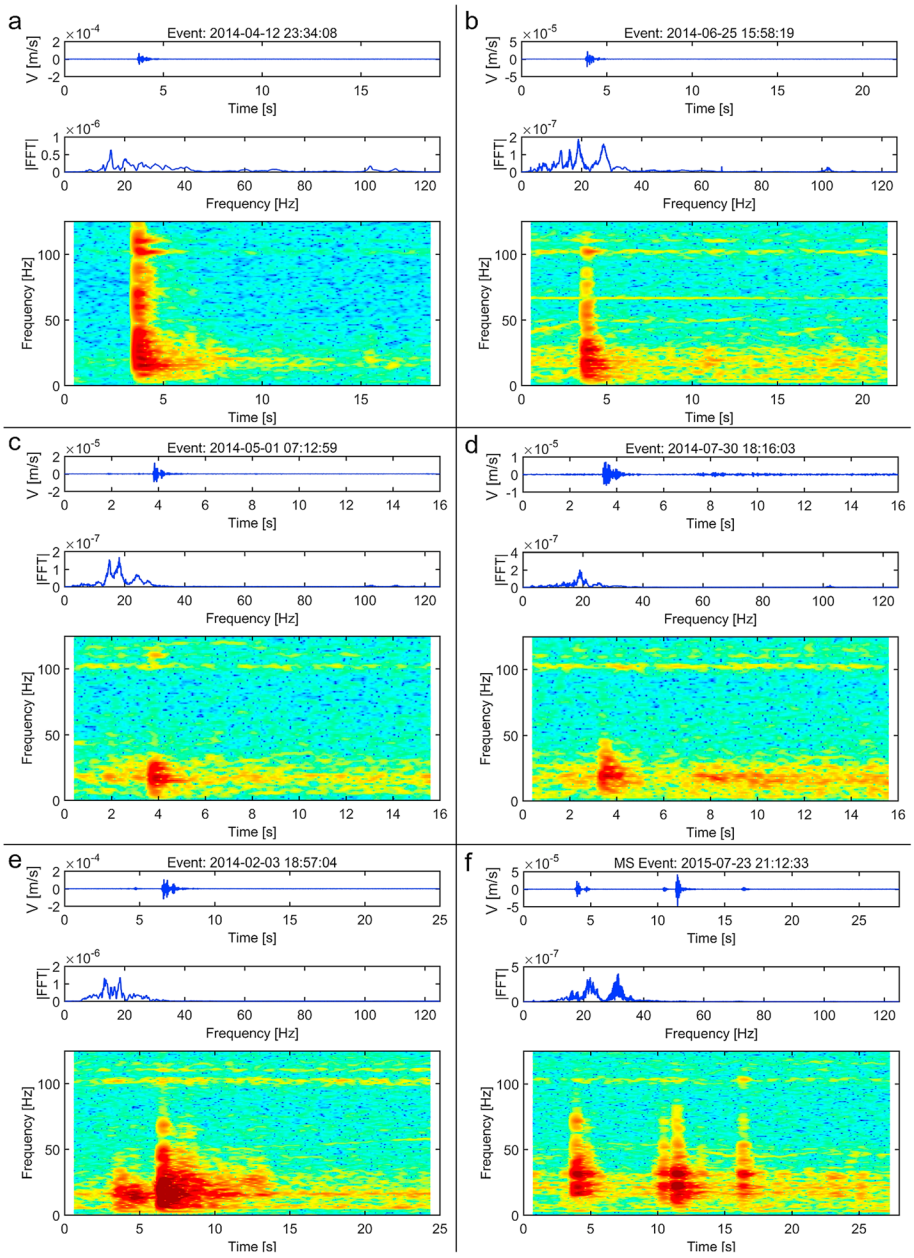

Figure 2. Examples of microseismic events recorded at Madonna del Sasso. In each section (a–f), from the top to the bottom: seismogram recorded on channel N of ST2, related Fourier spectrum and spectrogram.

stations located on block A (ST1, ST2, and ST3) were triggered, probably indicating MS sources located within the unstable volume but unable to reach station ST4 outside the fractured zone. Given the poor geometry of the monitoring network, no further source information could be inferred for all these events.

The nonlinear probabilistic location procedure was consequently carried out on a limited subdata set of 451 events (25% of the acquired MS events) recorded at all the four stations. For these MS events, location results are reported in Figure 3. Given the high number of events in a small volume, 68% confidence ellipsoids are shown instead of the complete 3-D PDF scatter clouds (Figure 3a). Ellipsoid semiaxial lengths vary from 3 to more than 20 m, reflecting uncertainties in the location procedure. However, the related ellipsoids are well contained within the rock mass confirming the origin of the events within the unstable

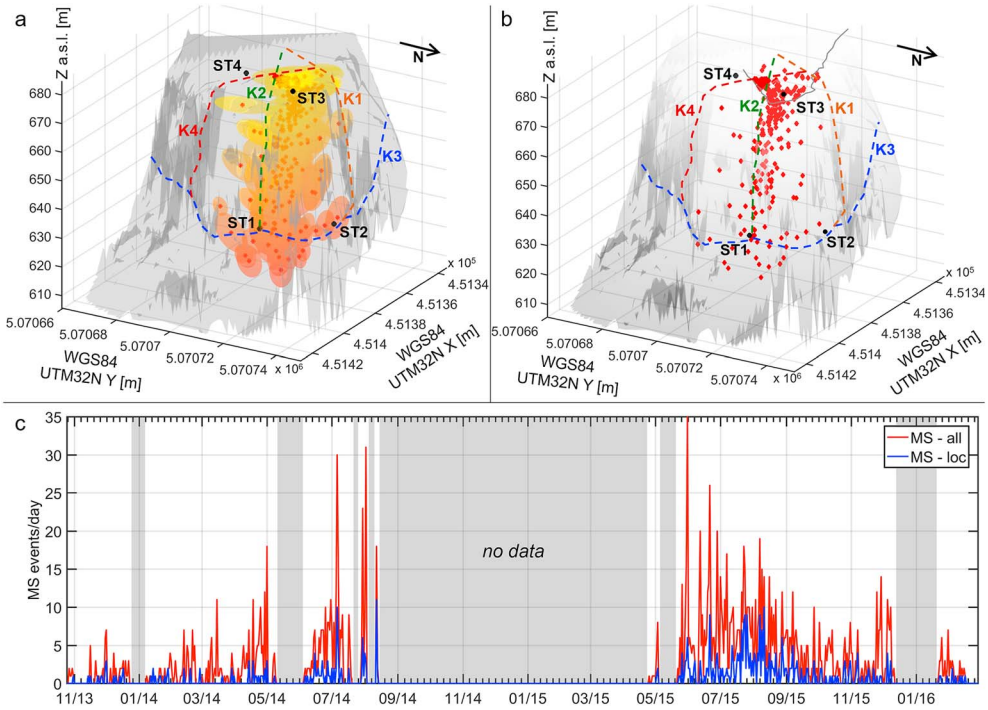

Figure 3. MS-event location. (a) 68% confidence ellipsoids referred to the location of 451 MS events. Ellipsoids are plotted in color scale from yellow to red (from surficial to deep events). The center of each ellipsoid is the Gaussian Expectation E(x), marked with the red asterisk. (b) Three-dimensional view of the maximum likelihood solutions (optimum hypocenter location, plotted with red diamonds) for the same events. (c) Daily number of total and located MS events.

compartments. Hypocenters related to the maximum likelihood solutions (Figure 3b) mainly locate the sources of these MS events along fracture K2, with a higher concentration in the first 10 m depth, particularly between the K2 and K4 intersection. Occasional deeper MS events are also observed around the basal fracture K3.

2.4. MS Data Set: Correlation With External Factors

Since waveform analysis and location results confirmed the fracture-related nature of the detected MS events, the temporal distribution of the site microseismicity was investigated as a function of the external factors potentially influencing the stability of the cliff.

The daily MS-event rate (Figure 3c) did not highlighted an irreversible increase in microseismicity over the monitored period, possibly indicating an acceleration to failure. Conversely, it is affected by reversible seasonal fluctuations, with a maximum activity during summer months (July–August, up to 30 MS events/day) and a minimum activity in cold months (January–February, approximately 2 events/day). Considering the results of the past displacement monitoring campaigns at the site, microseismicity seems therefore to increase in the periods in which the rock mass undergoes thermal expansion and progressive fracture closing, while few events are recorded during thermal contraction periods with associated fracture opening. Beside this seasonal-scale observations, the possible short-term influence of air temperature on the MS-event rate was further investigated.

Air temperature measurements were available on site for the period between January and April 2014. Temperature probes were located on the south and north faces of the cliff, and in the open fracture K2 at a depth of 10 m. Unfortunately, these three sensors were damaged few months after their installation. On-site temperature data are therefore available only for cold months, in which the number of recorded events is significantly lower than in warm months (Figure 3c). Temperature data over the whole period (November 2013 to February 2016) are thus referred to the meteorological monitoring station of ARPA Piemonte, located in Cesara (6 km north of the site, at a comparable altitude and on the same shore of the lake). Rainfall amounts have been also considered from the same meteorological station.

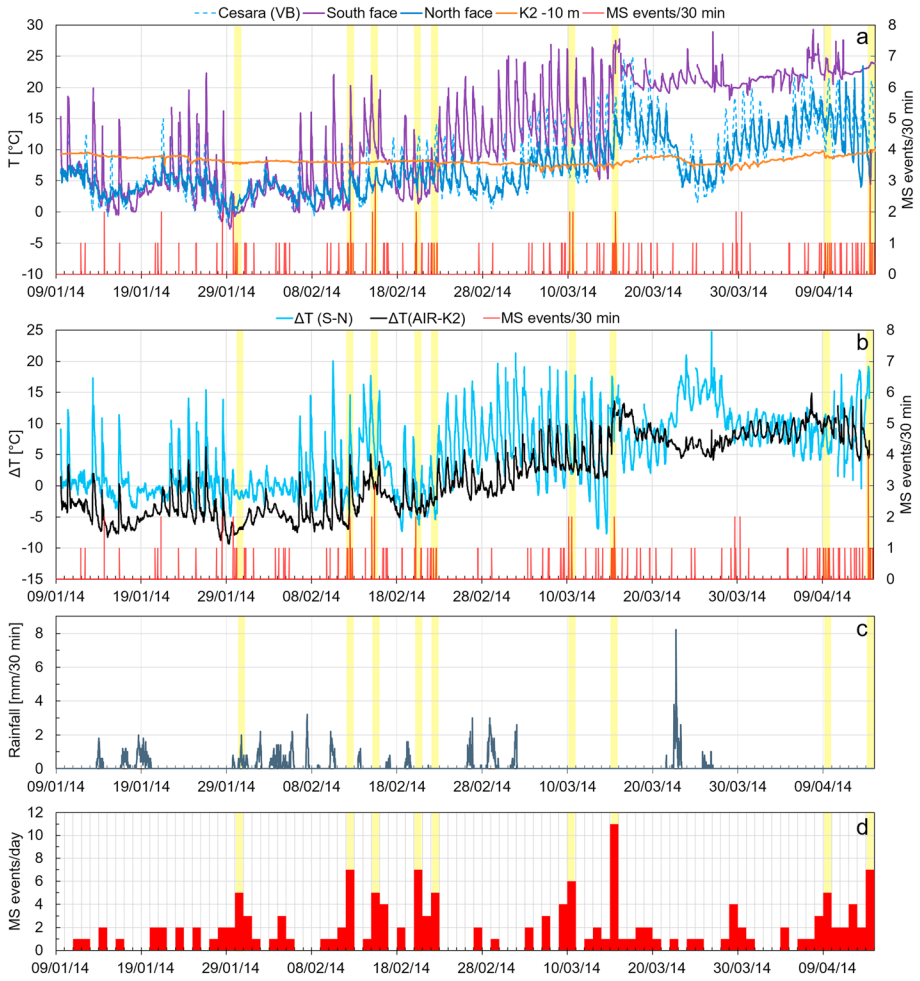

Figure 4. (a) Thirty-minute air temperature recorded by three on-site temperature probes (north face, south face, 10 m depth in fracture K2) and the reference meteorological station of Cesara (ARPA Piemonte) for the period January–April 2014. (b) Related average temperature and temperature difference computed between the south and north faces of the cliff and between the average of the two faces and the deep probe in fracture K2. In Figures 4a and 4b, the 30 min MS event rate is shown for comparison. (c) Thirty-minute rainfalls during the same period, from the meteorological station of Cesara (ARPA Piemonte). (d) Daily MS-event rate. Days with more than five MS events are highlighted in all the sections.

Temperature data from the on-site probes are reported in Figure 4a, in comparison with the data from the meteorological station of Cesara. A similar short- and long-term trend between the north face and the reference station is found, thus partially allowing further comparison in the periods without on-site data. Over the considered period, the south face of the cliff exhibited the highest air temperature fluctuations, with up to 20°C of variation in the same day (Figure 4a). The average trend for the north-face temperature is similar to the south until mid-February. After this date, the two temperature curves start to diverge. Also inner temperature measurements in fracture K2 are partially influenced by external fluctuations of the air temperature. Daily and seasonal temperature variations similar to the external probes, even if reduced, are observed (Figure 4a), thus confirming the significant opening and persistence, with intense air circulation detected on site.

Over this period, the highest daily peak of MS-event occurrence (15 March 2014, 11 events, Figure 4d) is observed in correspondence to the first rapid increase in both the external and internal temperature measurements (Figure 4a). As shown in Figure 4b, this day is also located on a sudden temperature rise, from the highest negative temperature difference between south and north faces (−8°C) to a significant positive difference (+18°C). All the other major daily peaks (≥ 5 events) are associated to rapid temperature changes, particularly as they concentrate during or immediately after periods in which the temperature difference between the south and north faces rapidly switches from negative

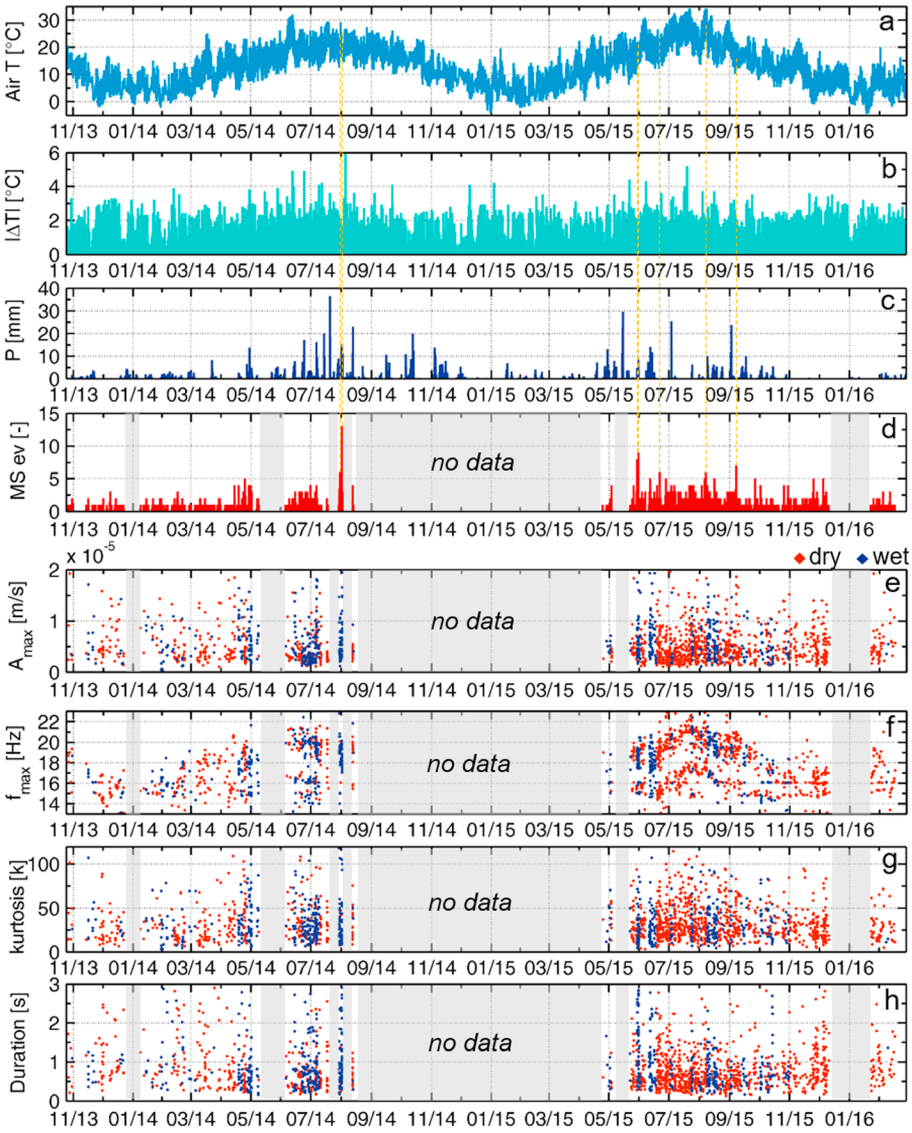

Figure 5. (a) Thirty-minute air temperature at the meteorological station of Cesara (ARPA Piemonte), in the period November 2013–February 2016. (b) Absolute value of thermal excursion between subsequent 30 min measurements. (c) Thirty-minute rainfalls recorded at the same location. (d) Thirty-minute number of MS events recorded on site. From Figures 5a–5d vertical dashed lines highlight the half-hours with more than five events (summarized in Table 1). (e) Maximum amplitude, (f) maximum frequency peak, (g) kurtosis, and (h) duration of the recorded MS events (recorded in dry and wet conditions, in red and blue respectively).

to positive values or shows sudden modifications due to the different insolation of the two sides of the cliff. The difference between air temperature (average of north and south face) and the deep temperature inside fracture K2, besides showing an increase from mid-March, is generally more stable than the temperature difference measured between the north and south faces (Figure 4b). Daily MS-event peaks are recorded when inner temperature is both higher or lower than external temperature. The increase in MS activity seems therefore to be mainly driven by sudden temperature variations between the sides of the cliff, leading to a consequent modification of the thermal gradient within the rock mass.

None of the MS peaks has associated significant rainfall amounts (Figure 4c). The only exception is the recording during 30 January 2014 (5 events), when precipitations occurred in concomitance with temperature below 0°C, which could have caused local ice formation in the preexisting fractures. The most relevant rain event in this period (23 March 2014) has, however, no relevant associated MS activity.

Table 1
Thirty-Minute Time Windows Showing Clusters of More Than 5 MS Events and Related Relationship With the Rainfall Amount and Temperature Variations in the Half Hour Before and After the Reported Start Time

Date (dd/mm/yyyy)	Start time (hh:Mm:Ss)	MS events/ 30 min	Rainfall/ 30 min (mm)	ΔT_{ST-30} (°C)	ΔT_{ST+30} (°C)
31/07/2014	17:00:00	6	8	−1	+0.6
01/08/2014	00:30:00	13	14	−0.2	−0.6
29/05/2015	21:00:00	8	5	−1.4	0
31/05/2015	01:00:00	9	8	−0.4	+0.8
21/06/2015	21:30:00	6	0	−0.6	−1
08/08/2015	01:30:00	6	0	0	−0.8
07/09/2015	13:30:00	7	0	+1.8	−0.4

Unfortunately, no information on the temperature difference between the two faces of the cliff was retrieved in the long-term period. In Figure 5 both temperature/rainfalls (in a and c) from the meteorological reference station and MS-event occurrence (in d) are shown for the whole monitored period at simultaneous 30 min sampling intervals. The absolute temperature difference of each half-hour with respect to the previous is shown in Figure 5b to globally highlight marked air temperature fluctuations. The computed half-hour average temperature excursion is ±0.4°C.

All the detected seven half-hours exceeding 5 MS events (summarized in Table 1) are located in warm months. Six of these peaks are recorded at night or in late afternoon. Most of the peaks are related to temporal temperature differences (recorded during the half-hour or in the previous 30 min) higher than the average value computed over the whole period. Additionally, comparing Figures 5b and 5d, half-hours exhibiting more than 4°C of temperature variation are always accompanied by microseismicity, even if the number of events does not always exceed 5. The increase in MS activity along the whole monitored period is therefore confirmed to be related to sudden temperature variations.

Four of the main peaks (Table 1) are also associated to rainfalls. The highest precipitation peak (14 mm) corresponds to the maximum MS-event occurrence (13 events). Comparing Figures 5c and 5d, the highest MS peaks are found after intense or long-lasting periods of precipitation. This fact partially contrasts with what is observed in the shorter time window related to the cold months (Figure 4). Taken together, these observations can suggest a combined contribution of temperature (sudden spatial and temporal gradients) and rainfall to the microseismicity of the site.

Characterizing parameters of the recorded MS events are summarized in Figures 5e–5h, in order to investigate possible variations in maximum amplitude, frequency peak in the Fourier spectrum, kurtosis, and duration between events occurring in dry or wet conditions. The threshold to distinguish events occurring in wet conditions was fixed to a minimum of 5 mm of rain cumulated within 2 days before the event start time. No significant changes in the parameters are observed between events occurring in dry or wet conditions. Conversely, a strong air temperature control on the peak frequencies in the Fourier spectra of the recorded events (Figure 5g) is identified, as already highlighted for ambient noise resonance frequencies in Colombero et al. (2017). Air temperature and frequency fluctuations are almost in phase, with maximum frequency during the hottest hours and lower values in cold periods. Also maximum-amplitude and kurtosis values seem to be weakly correlated to temperature fluctuations.

3. Microseismicity at the Laboratory Scale

3.1. Experimental Procedure and Equipment Versus Field Stress Conditions

Since spatial and temporal temperature variations within the rock mass were recognized to be the main potential governing factors of the cliff microseismicity, intact rock samples of the same lithology (*Granito di Alzo*) were selected from a quarry nearby the test site, to perform AE laboratory tests. As already mentioned in section 1, laboratory testing has the advantage of controlled boundary conditions, which can help to better constrain the link between external modifications and fracturing processes, investigating the related AE activity. Conversely, the need of maintaining the samples within a confined testing apparatus can give rise to different stress conditions with respect to the near-surface site conditions. At the field scale, loading conditions are indeed essentially controlled only by gravity, with superimposed stress and strain fluctuations driven by external factors or internal fluid pressure. The adopted laboratory procedure was thus chosen as a compromise between the available testing instrumentation and the need of studying the effect of temperature ramps on fractured samples, using concomitant AE recordings as a proxy to field-scale microseismicity. The experiments were conducted both in dry and saturated conditions, to further explore the influence of fluids on the sample behavior during the heat treatment.

Tests were performed using a servo-controlled triaxial apparatus (TRI-X 100 MPa/200°C, Sanchez Technologies), with an actuator providing axial stress (σ_1, up to 680 MPa) and confining pressure ($\sigma_2 = \sigma_3$, up to 100 MPa) applied via silicone oil using syringe pumps. An independent pressurization system controls the pore pressure for sample saturation. An external furnace applies temperatures up to 200°C. The tested rock sample consisted of a cylindrical intact rock sample of 40 mm diameter and 100 mm length separated from the confining medium by an engineered rubber jacket (Sammonds, 1999). The jacket is fitted with 12 ports for installing an array of 12 piezoelectric transducers (1 MHz central frequency) to record the AE activity during the test (at a sampling frequency of 10 MHz). The system was also set to perform an active survey across the sample every 2 min by pulsing each of the 12 sensors in sequence with a 200-V pulse, while the remaining 11 functioned as receivers. The waveforms of each survey were stored to enable first-arrival-time picking and the construction of the evolving velocity model of the sample, a fundamental requirement for hypocenter location of the detected AEs.

The first preliminary test phase involved generation of fractures within all the samples. Samples were deformed until rupture at a constant axial strain rate of $5 \cdot 10^{-6}$ s^{-1}, controlled via linear variable displacement transducers. Two types of experiments were carried out: "dry" tests, that is, confining pressure of 2 MPa and no pore pressure (samples G1, G2, and G5), and "wet" tests, that is, water-saturated experiments with a constant pore fluid pressure (deionized/distilled water) of 0.5 MPa and a confining pressure of 2.5 MPa (samples G3 and G4). We underline that laboratory loading conditions during this phase are different from the site conditions that have led to fracture formation. This laboratory test phase was, however, necessary to obtain fractures within the samples and to obtain reference AE waveforms and spectrograms of the microcracking processes, for a reliable validation of the AE waveforms recorded during the second phase. Even given the different failure conditions between laboratory and site during this phase, confining pressures were kept low (2 MPa, approximately 80 m depth) to reflect the near-surface circumstances in which fractures could probably have formed.

After failure, temperature ramps were applied to samples G5 (dry test) and G4 (wet test). In this second phase, the postfailure differential stress ($\sigma_1 - \sigma_3$) was set to the 75% of its residual value, to reduce marked loading conditions and enable possible thermal expansion of the samples both in axial and radial directions. Setting the differential stress to a constant value had the advantage to allow the sample to freely equilibrate according to the applied thermal variations and to balance and control its deformation, in order to avoid its slip along the fracture plane, leading to the test failure. Maintaining these conditions, the two samples were therefore heated from room temperature (~27°C) up to 65°C. Temperature was applied to the upper surface of the cylindrical samples and progressively propagated within the sample volume. Measurements at the top and bottom surfaces of the samples were performed every 3 s (same sampling rate of the mechanical parameters), thus providing an estimation of the thermal gradient across the sample during the whole test duration. Both samples were maintained at the upper target temperature for 15 min and then left cooling down to the original ambient temperature. The heating rate was +0.4°C/min from room temperature to 50°C for both samples, followed by +0.15°C/min for the dry (G5) test and +0.2°C/min for the wet (G4) test from 50°C to 65°C. Both samples cooled down to room temperature at an average rate of −0.15°C/min. Due to technical limitations, it was not possible to test the samples at temperature lower than the room temperature, to have a full comparison with the range of temperature variations detected on site.

3.2. AE Processing Methods

Similar to field MS data set, AE processing firstly involved spectral analysis and source location of the recorded waveforms. AE source location was attempted to compare a representative data set of events occurring during both the failure and heating stages of the dry (G5) and wet (G4) tests. The evolving velocity model of each sample was reconstructed from the active surveys performed every 2 min across the specimens during the whole duration of the tests. A transversely isotropic location algorithm was used for the AE events showing accurate first-arrival-time picking on at least 6 of the 12 recording channels.

In addition, the same parameters computed for the MS events (maximum amplitude, frequency peak in the AE-event Fourier spectrum, kurtosis, and duration) were computed for all the AEs having a clear onset on at least six channels, in order to avoid disturbances and transients. Analyses on the temporal variation of these parameters as a function of external factors were undertaken to gain insight on the sample behavior and to provide comparison and support to the interpretation of the field-scale microseismicity.

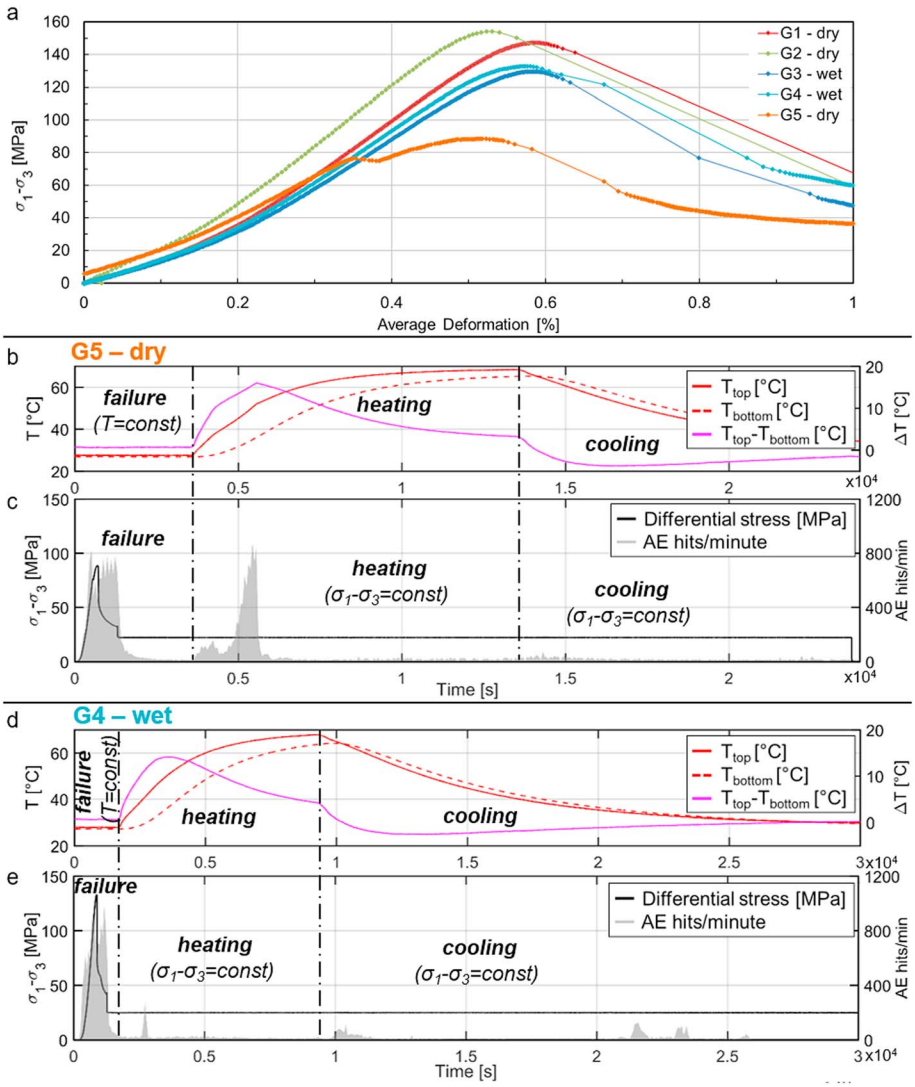

Figure 6. (a) Stress-strain curves from the preliminary failure stages of all samples. G5 dry test: (b) temperature of the top and bottom surfaces of the sample and related temperature difference; (c) differential stress and AE-hit rate during the test. G4 wet test: (d) temperature of the top and bottom surfaces of the sample and related temperature difference; (e) differential stress and AE-hit rate during the test.

3.3. AE Results: Spectrograms and Source Location

Stress-strain curves for the five experiments are shown in Figure 6a. For the water-saturated samples (G3 and G4), a lower strength is noted at approximately 130 MPa compared to the dry samples G1 and G2 of approximately 150 MPa axial stress. These results highlight a strength reduction driven by water, which enhances crack nucleation and propagation. A slightly different behavior is evident for sample G5, which exhibited a minor peak before the final failure and a significantly lower peak strength (maximum axial stress of less than 90 MPa). This behavior is likely due to preexisting fractures within the sample, which contributed to significantly decrease its final strength, and is considered an outlier to the set. However, such heterogeneity can also serve as evidence of the fracturing conditions of the investigated rock mass.

AE-hit rates throughout the tests are compared in Figures 6c and 6e, respectively, for samples G5 (dry) and G4 (wet). Thermal conditions along the test phases are reported in Figures 6b and 6d in terms of temperature values at the top and bottom surfaces of the samples, and temperature difference between the two faces. In the preliminary failure stage of both tests, as peak stress and sample failure were approached, the AE-hit rate increased entering the supraexponential phase (described by Benson et al., 2007). After failure, the AE-hit rate entered a period of quiescence (e.g., 2000–3500 s for G5) until the heating stage was activated.

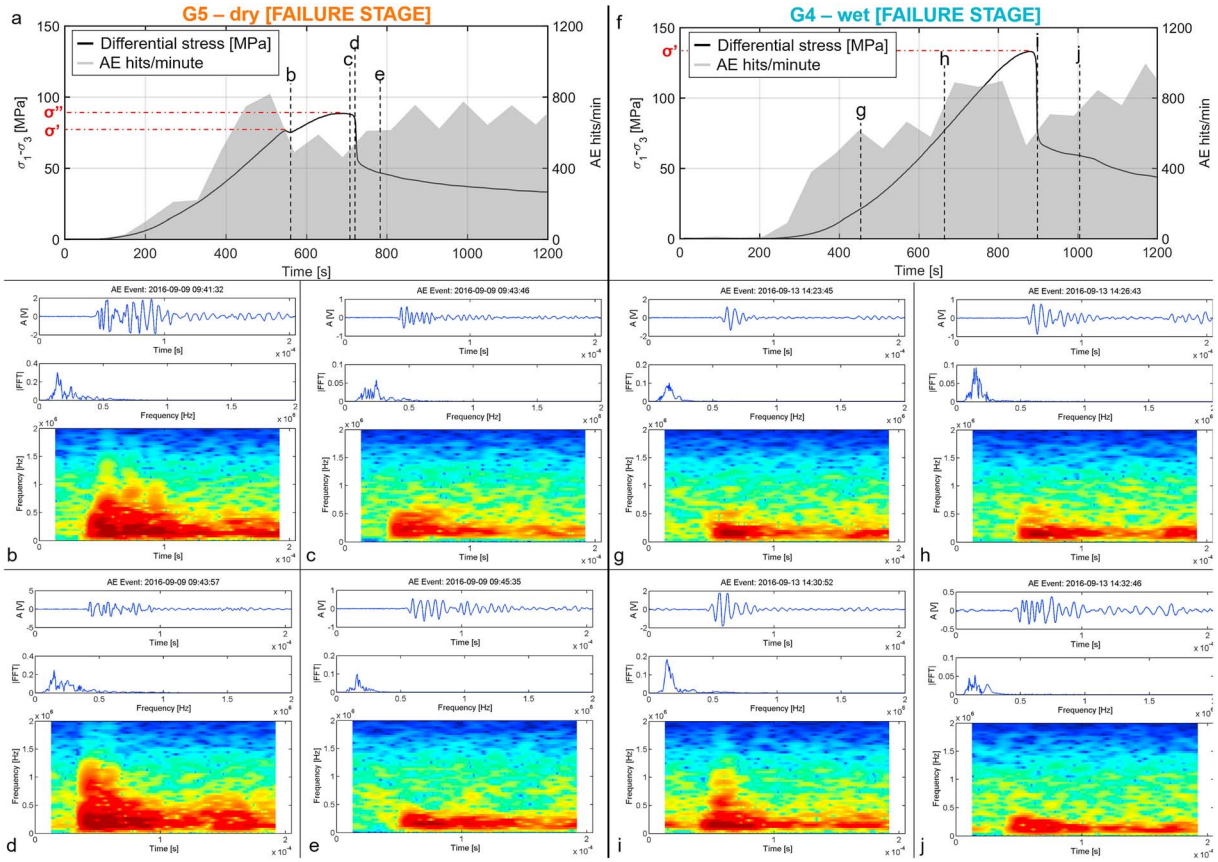

Figure 7. Failure stages of G4 and G5 triaxial tests. (a) AE hits/min and differential stress of G5 test (dry). (b–e) Selected representative AE events (waveform, Fourier spectrum, and spectrogram, from the top to the bottom of each section), event occurrence time is highlighted in Figure 7a with the vertical black dashed lines. (f) AE hits/min and differential stress of G4 test (wet). (g–j) Selected representative AE events (waveform, Fourier spectrum, and spectrogram, from the top to the bottom of each section), event occurrence time is highlighted in Figure 7f with the vertical black dashed lines. The temperature is constant (room temperature) during the failure stages of both tests.

During this phase, the AE activity picked up dramatically after 5,000 s for sample G5 (Figure 6b). The AE peaks correspond to the time at which the maximum temperature difference was measured between the two edges of the samples (16°C). This observation may indicate temperature-driven new microcracking of the sample. By contrast, fewer events were detected during the cooling stage of sample G5 (as seen from approximately 14,000 s) and during both the heating and cooling stages of sample G4 (Figure 6c).

During both tests, subtle but clear changes in the spectral content of the waveforms were also noticed. These are summarized for the different test phases in Figure 7 (failure stage), Figure 8 (initial heating stage, from room temperature to approximately 45°C), and Figure 9 (initial cooling stage, from 65°C to 50°C) as a function of either differential stress (for the failure stage at constant temperature) or temperature fluctuations (for the heating and cooling stage at constant differential stress).

In the failure stage of the dry test (Figure 7a), approximately the 60% of the recorded AEs show a high-frequency onset (e.g., Figures 7b and 7d, hereafter called HF), similar to the MS spectral shapes recorded on site. These are very energetic events that have been usually linked to fracturing/failure mechanisms driving the cracks growth and linkage into macroscopic fracture surfaces (Benson et al., 2010). In the remaining 40% of the recorded data set, the high-frequency onset is partially missing (e.g., Figure 7c), as also observed on site (Figures 2c and 2d), but still reflects the HF reference spectral shape. After failure, all the recorded events are low-frequency AEs (hereafter called LF, e.g., Figure 7e) that may be linked to stick slip along the generated macrofractures. In contrast, during the failure stage of the wet test (Figure 7f), with the exception of the clear HF AEs related to the final failure (Figure 7i), more than 95% of the recorded signals show less pronounced high-frequency onsets (e.g., Figures 7g and 7h). These spectrograms are more akin to

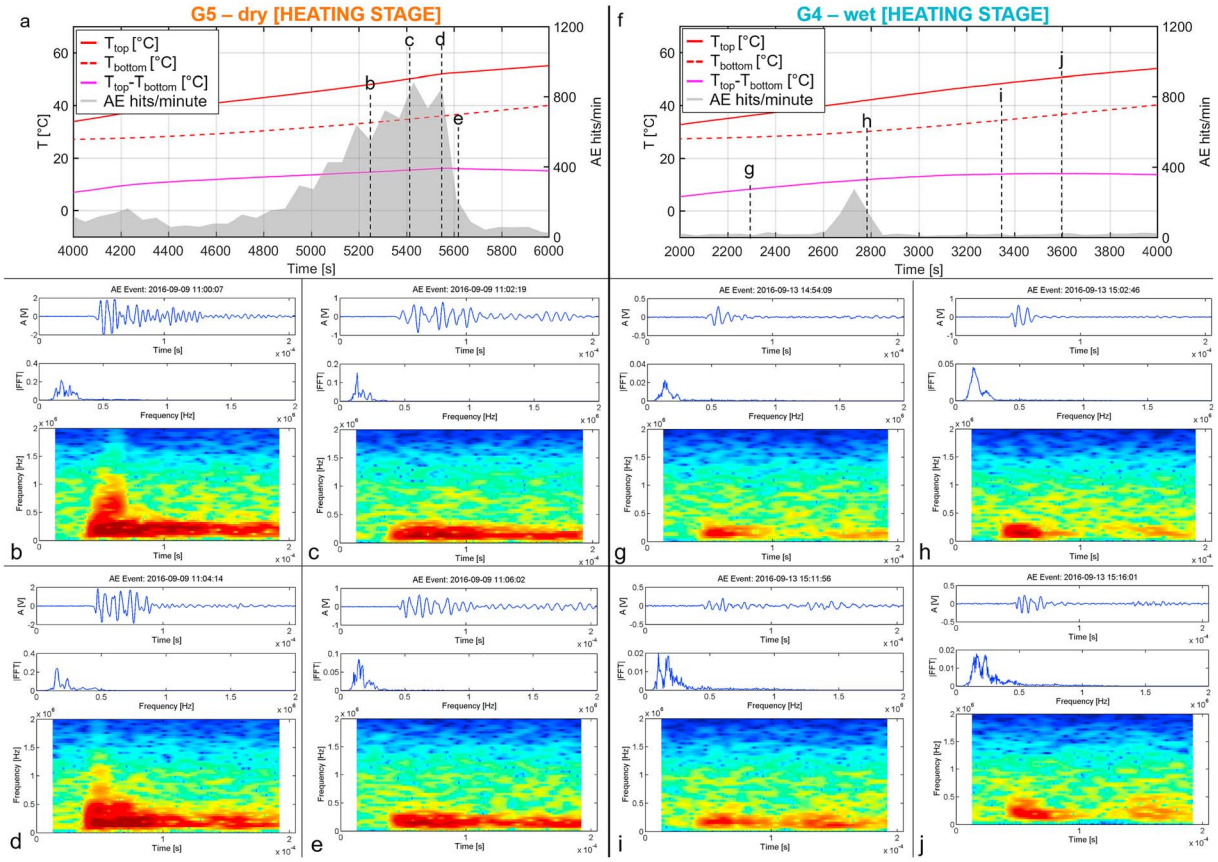

Figure 8. Heating stages (from room temperature to 40°C) of G4 and G5 triaxial tests. (a) AE hits/min and sample temperatures of G5 test (dry). (b–e) Selected representative AE events (waveform, Fourier spectrum, and spectrogram, from the top to the bottom of each section), event occurrence time is highlighted in Figure 8a with the vertical black dashed lines. (f) AE hits/min and sample temperatures of G4 test (wet). (g–j) Selected representative AE events (waveform, Fourier spectrum, and spectrogram, from the top to the bottom of each section), event occurrence time is highlighted in Figure 8f with the vertical black dashed lines. The differential stress is constant (75% of the residual value after failure) in both tests.

the LF frictional signals observed in the stick slip after failure (Figure 7j) and can be explained as "hybrid" events, with a less pronounced onset and a long lasting tail, caused by a combination of the opening of new cracks and pathways with the movement of the high-pressure pore fluid (Benson et al., 2010).

Many new HF events are recorded during the heating stage (Figure 8a) of the dry test (e.g., Figures 8b and 8d). These spectral shapes are common to approximately the 40% of the AEs recorded during the AE peak at 5,000–5,500 s. The remaining events show LF spectral shapes (e.g., Figures 8c and 8e). They represent approximately the 60% of the detected AEs during the AE peak and become the only dominant spectral shapes after it. Conversely, only a reduced number of LF events is recorded during the heating (Figure 8f) of the wet sample (Figures 8g–8j) with no associated HF events.

No HF-type events are detected during the cooling stage of the dry sample (Figures 9a–9e), while spectrograms of the wet sample (Figures 9f to 9j) are similar to the failure stage and could potentially indicate new damage within the sample.

The AE source location was obtained for 468 events of the dry test and 282 events of the wet test. Particularly, for the dry test, 258 located events are related to the initial failure stage (HF AEs) and 210 to the heating stage (73 AEs showing HF spectrograms and 137 AEs with LF spectral content). For the wet test, 222 and 50 located events were related to the failure and heating stages, respectively (with only 8 AEs showing HF features during the failure phase). As highlighted in Figure 10, complex fracture systems are generated from the deformation/failure process on both samples, roughly consisting in a conjugate system of two main fractures, with associated several microfractures. During the dry test (Figures 10a–10), failure-related AEs appear to originate within the most fractured areas, with two main clusters of events, roughly separated and

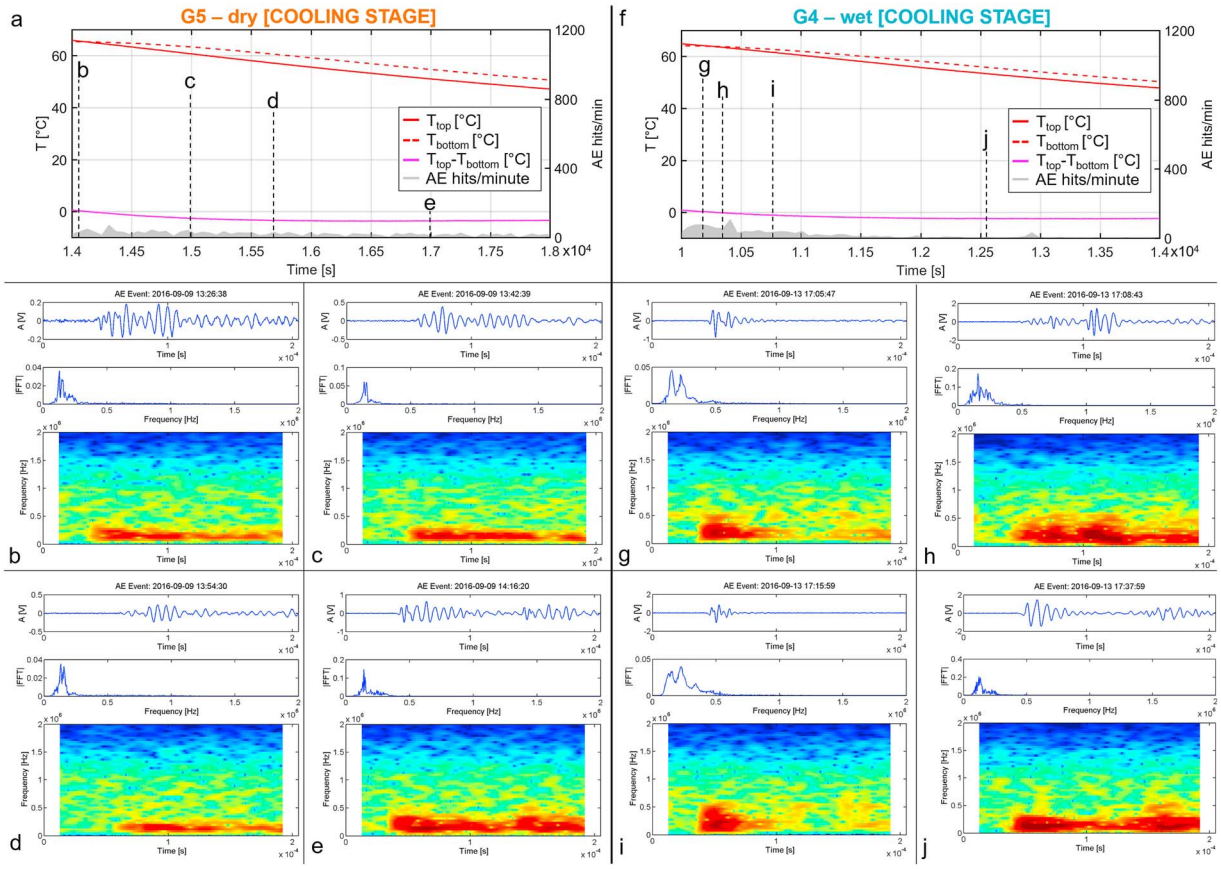

Figure 9. Cooling stages (from 65°C to 50°C) of G4 and G5 triaxial tests. (a) AE hits/min and sample temperatures of G5 test (dry). (b–e) Selected representative AE events (waveform, Fourier spectrum, and spectrogram, from the top to the bottom of each section), event occurrence time is highlighted in Figure 9a with the vertical black dashed lines. (f) AE hits/min and sample temperatures of G4 test (wet). (g–j) Selected representative AE events (waveform, Fourier spectrum, and spectrogram, from the top to the bottom of each section), event occurrence time is highlighted in Figure 9f with the vertical black dashed lines. The differential stress is constant (75% of the residual value after failure) in both tests.

centered along the vertical axis, in the lower and upper half of the sample, respectively. Heating-related AE sources are mainly located between these two clusters. For the wet test (Figures 10e–10h), a weaker correlation with the location of the macroscopic fracture traces is observed both for the failure- and heating-related events. This is likely to reflect the more intense pervasive microfracturing of the saturated sample driven by water pressure and flow.

3.4. AE Data Set: Correlation With External Factors

In order to gain further insight on the sample behavior, the same salient parameters computed for the MS field data set have been analyzed for the laboratory AEs, as a function of the external factors (stress drop and temperature) applied during the tests. AE maximum amplitudes, frequency peaks in the Fourier spectrum, kurtosis, and duration values are reported in Figure 11 for the failure stage and in Figure 12 for the heating/cooling stages of both the dry and wet experiments.

During the dry test, AE maximum amplitude is found to increase approaching both the first and the main stress drop related to the sample failure (related differential stresses are indicated with σ' and σ'', respectively, in Figure 11a). After failure, lower-amplitude values are found for the LF events associated to the postfailure stick slip. A new amplitude increase characterizes the beginning of the heating stage, most probably due to the formation of new microcracks, until probable fracture sealing caused by the thermal expansion of the sample (around t = 5,500 s from G5 test start time, corresponding to maximum temperature difference between the sample edges = 16°C, Figure 12a). After this peak, the temperature gradient starts to decrease, and high AE amplitudes are no longer detected, even during the cooling stage. Only a

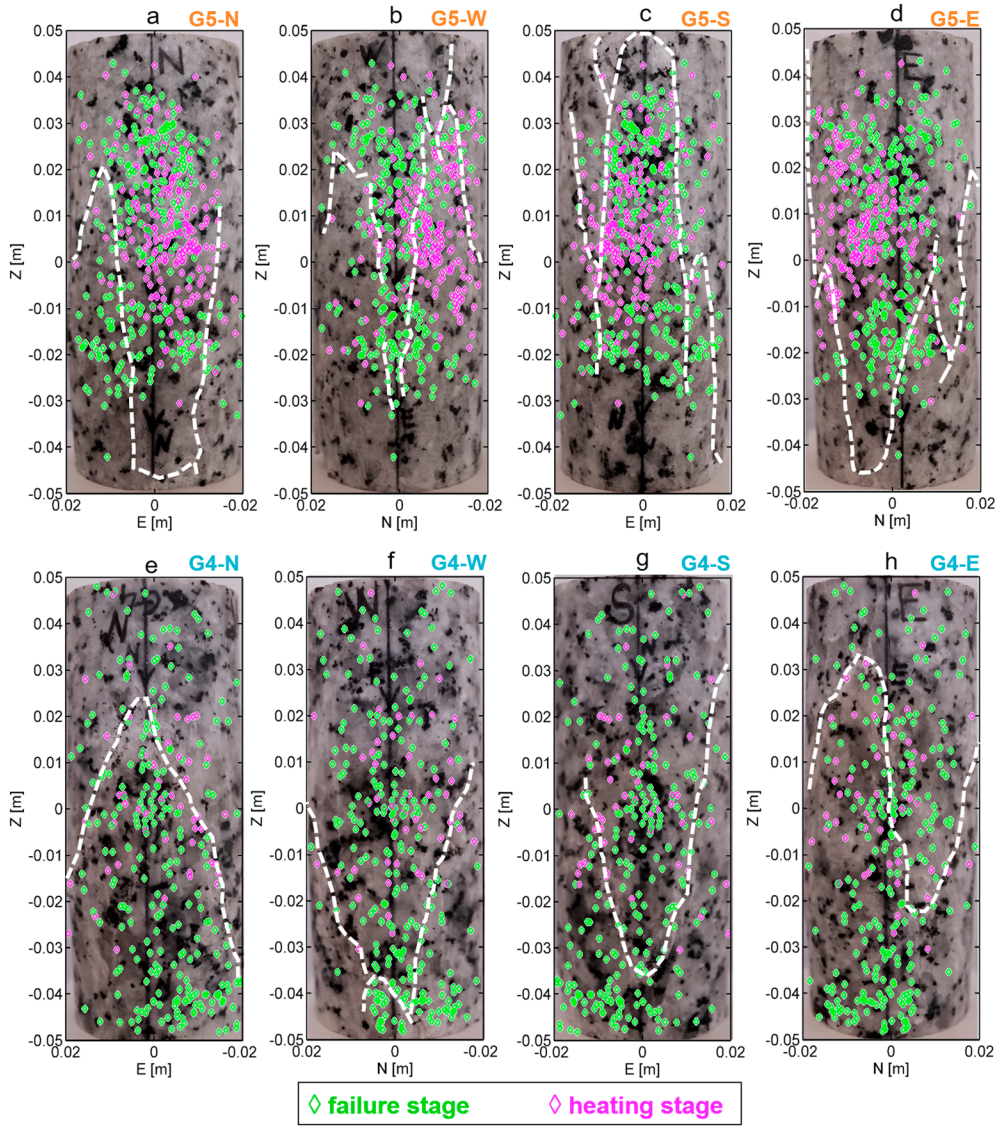

Figure 10. AE-event location. G5 dry sample, view of the 468 relocated events from the (a) north, (b) east, (c) south, and (d) west face. G4 wet sample, view of the 332 relocated events from the (e) north, (f) east, (g) south, and (h) west face. Green and magenta diamonds refer to the events that occurred during the failure and heating stage of each test, respectively. On each sample face, the macroscopic fracture traces are highlighted with the dashed lines.

few low-amplitude signals are recorded, probably due to gouge crushing and comminution linked to fracture closing/opening. The frequency behavior over time is even more significant in differentiating these two phenomena (Figure 11b). Before the first stress drop (σ'), frequency peaks of the HF AEs cluster around the mean values of both 242 kHz (highlighted with f′, in Figure 11b) and 154 kHz (f″, in Figure 11b). After σ', frequency peaks focused around f′ almost disappear. After the main stress drop (σ'') frequency peaks are centered around an even lower residual value (f_{RD} = 140 Hz, in Figure 11b). In the first heating stages, a new concentration of HF AEs is observed around f′ and f″, while after fracture sealing, the frequency peaks of the remaining few LF AEs remain centered on the residual value f_{RD}. Since kurtosis defines the "peakedness" of a signal, it may be an additional useful discriminatory parameter between LF stick slip waveforms (long duration and flat shape, with associated low kurtosis) and HF microcracking signals (shorter duration and sharper shape, with associated high kurtosis). The highest kurtosis values are recorded before σ' while are comparable in the time interval between σ' and σ'' (Figure 11c) and in the heating phase preceding fracture sealing (Figure 12c). Conversely, the AE durations are minimum before σ' (Figure 11d) and progressively increase after the first failure. Some events with

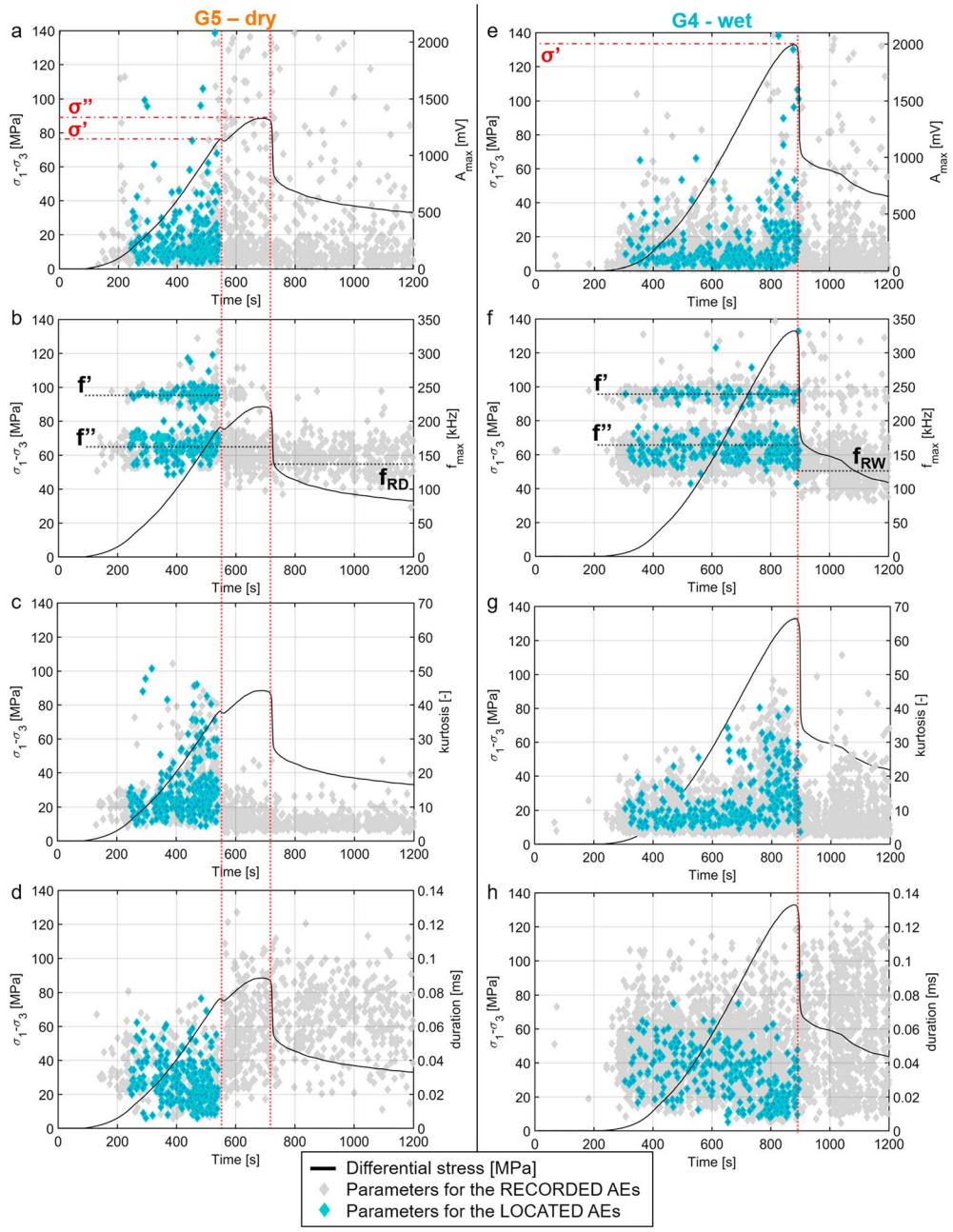

Figure 11. AE parameters during the failure stages of G5 (a–d) and G4 (e–h) tests. (a, e) Maximum Amplitude; (b, f) maximum frequency peak; (c, g) kurtosis value; and (d, h) duration. Gray and light blue diamonds refer to whole AE data set (events with clear onset on at least six channels) and the localized AE events, respectively.

short duration are detected in the heating stage before fracture sealing, while further heating and cooling events exhibit longer durations (Figure 12d).

The failure stages of the wet sample showed a similar behavior (Figures 11e–11h). Before failure, frequency peaks are centered on the same f′ and f″ average values found from the dry test, even if the majority of events exhibited LF spectral shapes (no high-frequency onset). A clear frequency cutoff is noticed at σ'. After failure, frequency peaks are located around the residual wet value of 127 Hz (f_{RW} in Figure 11f), thus slightly lower than the dry f_{RD} value (Figure 11b). No clear clustering of the parameters is observed during the heating/cooling stages of the wet test (Figures 12e–12h). Fluid circulation is therefore likely to have inhibited fracture sealing associated to the sample thermal expansion.

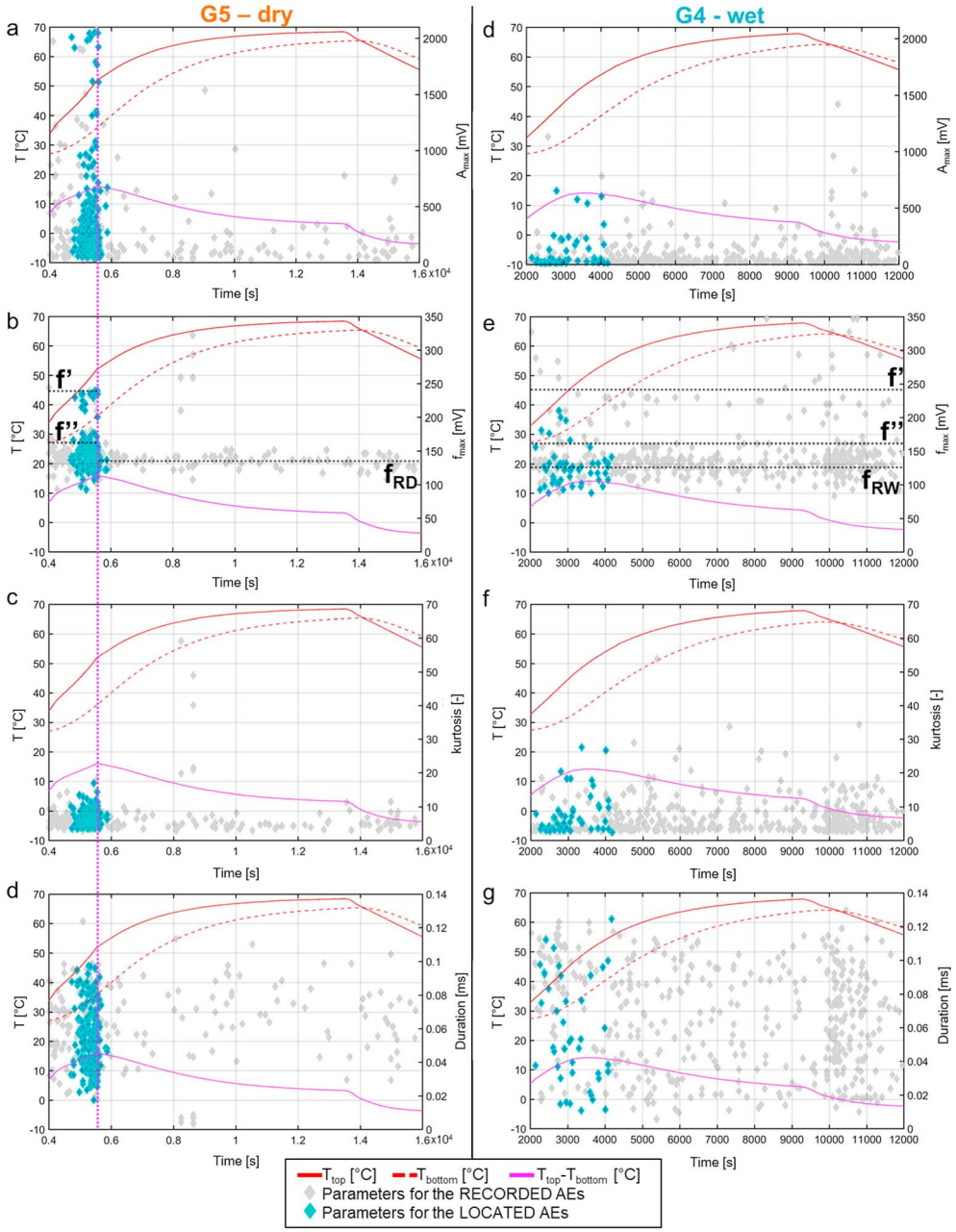

Figure 12. AE parameters during the heating/cooling stages (from room temperature to 65°C/from 65°C to 60°C) of G5 (a–d) and G4 (e–h) tests. (a, e) Maximum Amplitude; (b, f) maximum frequency peak; (c, g) kurtosis value; and (d, h) duration. Gray and light blue diamonds refer to whole AE data set (events with clear onset on at least six channels) and the localized AE events, respectively.

4. Discussion and Conclusions

Our analysis of the seismic data set recorded at the potentially unstable cliff of Madonna del Sasso revealed the presence of several MS events during the monitored period. Dealing with the site stability, it must be highlighted that the recorded microseismic activity is limited (1,773 MS events in almost 18 monitored months) and involves no irreversible acceleration in the MS-event rate. Both MS waveform analysis and source location highlighted, however, the fracture-related nature of the detected events. In particular, MS events exhibited peculiar spectral characteristics (HF onset with rapid exponential decay) that have been usually related in literature to microcracking processes or small-scale slips along fractures. Due to the poor geometry of the network, source information was only retrieved for the MS events that were recorded at

all the four monitoring stations (25% of the data set). These events clustered in the shallower parts of fracture K2, separating the two unstable blocks, or at the intersection between fractures K2 and K4. Approximately 45% of the events were, however, recorded only by the stations placed at the foot of block A, indicating low-energy microseismicity also at the base of the unstable compartment.

The long-term temporal evolution in the MS rate highlighted reversible seasonal fluctuations, with summer peaks of more than 30 MS events/day reduced to lower daily rates (around 2–5 MS events/day) in colder months. Past displacement monitoring measurements at the site (Regione, 1993) highlighted similar reversible modifications in fracture openings due to the seasonal thermal dilation of the rock mass. Colombero et al. (2017) detected coherent temperature-driven seasonal reversible variations in the resonance frequencies of the unstable blocks from ambient seismic noise recordings. The detected MS activity seems therefore emphasized during the periods of rock mass thermal expansion.

The short-term temporal evolution in the MS rate was coherently recognized to be mainly driven by temperature. Sudden air temperature variations (temporal gradient) or marked temperature differences between the cliff's faces (spatial gradient) were interpreted to cause differential thermal dilation and induce thermal stresses leading to microcracking processes within the cliff, as already demonstrated by Gunzburger et al. (2005).

The field results showed further similarities with the experiments carried out by Garbini (2009), Swami (2011), and Warren et al. (2013) on decimetric granitic boulders. These boulders can be considered as a mesoscale unfractured reproduction of the granitic cliff. In particular, Swami (2011) correlated the majority of the recorded AEs with sudden variations in temperature, caused by either different insolation of the boulder faces (particularly, evident in late afternoon and evening hours) or rapid global changes in solar radiation, due to cloud movement or to a modification in the wind speed and direction. These sudden temperature variations caused thermal contraction and expansion of the boulders (measured with independent strain gauges). In addition, a prominently larger number of AE sources were located on the top of the investigated boulders, while very few events occurred in their bottom part. In the upper hemisphere of each boulder, the densest hypocenter locations clustered along the east-west central line due to differential insolation of the top-bottom and south-north faces. Interestingly, the observed distribution of MS-event source locations at the cliff scale perfectly compare with these observations.

Considering rainfall and moisture content, during the experiment of Swami (2011) the largest number of AE events occurred during precipitation or when the monitored boulder was wet. However, precursor events often preceded the start of rainfall time, probably due to the concomitant meteorological and temperature changes. Coherently, on the longer term, rainwater seems to play a role in promoting microcracking also at the studied cliff but interpreted only in the direction of inducing or accelerating thermal variations and gradients within the rock mass.

To better focus on the role of temperature in rock fracturing, a laboratory procedure was designed, enabling to study the effect of temperature ramps on fractured samples. As discussed earlier, some necessary variations between the site and laboratory test settings still remain due to the need of reproducing in a confined cell the near-surface free conditions of the cliff. Nevertheless, a significant AE activity driven by thermal stresses was recorded during the after-failure heating phase of the dry sample. Particularly, the peak of AE occurrence was coincident with the major temperature difference between the two faces of the sample, reflecting site observations. Despite the different scale of observation, and thus the dominant frequency of the events, HF thermal cracking AEs showed spectral shapes consistent with HF rupture cracking recorded during the preliminary failure stage of the samples. This provided the final evidence of the thermal cracking nature of the signals recorded on site. Conversely, few HF events were observed during the laboratory tests performed in wet conditions. For this last test the majority of the events was indeed of LF type underlining the effect of pore water in the sample. The absence of a significant number of LF events in the field MS data set, commonly used to indicate fluid or frictional processes, further suggests a minor role of pore water content and water movement along fractures on the site microseismicity. This final consideration is also confirmed by the spectral and parametric similarities of the MS events recorded at the site during both dry and wet periods. It is likely that the amount of rainwater and the steep morphology of this rock mass do not allow for a significant saturation of the material and related pore fluid/rock matrix interactions. In addition, water movements within the existing fractures are not particularly forced due to their significant openings. The role of rainfall may therefore consist more in enhancing any sudden temperature variation, accelerating thermal

modifications, than in saturating the rock mass. More attention must be, however, dedicated to periods with concomitant precipitation and air temperature below 0°C. It indeed observed a slight increase in the MS activity with these conditions, probably indicating freezing-induced stresses.

The combined MS/AE approach has thus elucidated our understanding of very shallow thermal-related mechanisms driving the microseismicity at the unstable rock mass, trying to bridge the gap between the two investigation scales.

Acknowledgments
This work was partially funded within Progetto d'Ateneo 2012 - SAFER of Università degli Studi di Torino: "Detecting slow deformation signals preceding dynamic failure: A new strategy for the mitigation of natural hazards" (grant TO_Call2_2012_0057). The reference MS/AE data set from site monitoring and laboratory tests can be downloaded from https://www.researchgate.net/publication/317951053_MSAE_dataset_Madonna_del_Sasso (DOI: 10.13140/RG.2.2.19397.65763). Please contact the corresponding author for further material or information on the data set.

References

Amitrano, D., Arattano, M., Chiarle, M., Mortara, G., Occhiena, C., Pirulli, M., & Scavia, C. (2010). Microseismic activity analysis for the study of the rupture mechanisms in unstable rock masses. *Natural Hazards and Earth System Sciences*, *10*(4), 831–841. https://doi.org/10.5194/nhess-10-831-2010

Amitrano, D., Grasso, J. R., & Senfaute, G. (2005). Seismic precursory patterns before a cliff collapse and critical-point phenomena. *Geophysical Research Letters*, *32*, L08314. https://doi.org/10.1029/.%202004GL022270

Amitrano, D., Gruber, S., & Girard, L. (2012). Evidence of frost-cracking inferred from acoustic emissions in a high-alpine rock-wall. *Earth and Planetary Science Letters*, *341–344*, 86–93. https://doi.org/10.1016/j.epsl.2012.06.014

Benson, P. M., Thompson, B. D., Meredith, P. G., Vinciguerra, S., & Young, R. P. (2007). Imaging slow failure in triaxially deformed Etna basalt using 3D acoustic-emission location and X-ray computed tomography. *Geophysical Research Letters*, *34*, L03303. https://doi.org/10.1029/2006GL028721

Benson, P. M., Vinciguerra, S., Meredith, P. G., & Young, R. P. (2008). Laboratory simulation of volcano seismicity. *Science*, *322*(5899), 249–252. https://doi.org/10.1126/science.1161927

Benson, P. M., Vinciguerra, S., Meredith, P. G., & Young, R. P. (2010). Spatio-temporal evolution of volcano seismicity: A laboratory study. *Earth and Planetary Science Letters*, *297*(1-2), 315–323. https://doi.org/10.1016/j.epsl.2010.06.033

Boriani, A., Burlini, L., & Sacchi, R. (1990). The Cossato-Mergozzo-Brissago line and the Pogallo line (southern alps, N-Italy) and their relationship with the late-Hercynian magmatic and metamorphic events. *Tectonophysics*, *182*(1-2), 91–102. https://doi.org/10.1016/0040-1951(90)90344-8

Boriani, A., & Giobbi, E. (2004). Does the basement of western alps display a tilted section through the continental crust? A review and discussion. *Per Mineral*, *73*(2), 5–22.

Browning, J., Meredith, P., & Gudmundsson, A. (2016). Cooling dominated cracking in thermally stressed volcanic rocks. *Geophysical Research Letters*, *43*, 8417–8425. https://doi.org/10.1002/2016GL070532

Burdine, N. (1963). Rock failures under dynamic loading conditions. *Society of Petroleum Engineers Journal*, *3*(01), 1–8. https://doi.org/10.2118/481-PA

Burlini, L., Vinciguerra, S., Di Toro, G., De Natale, G., & Burg, J.-P. (2007). Seismicity preceding volcanic eruptions: New experimental insights. *Geology*, *35*(2), 183–186. https://doi.org/10.1130/G23195A.1

Caplan-Auerbach, J., & Huggel, C. (2007). Precursory seismicity associated with frequent, large ice avalanches on Iliamna Volcano, Alaska. *Journal of Glaciology*, *53*(180), 128–140. https://doi.org/10.3189/172756507781833866

Colombero, C., Comina, C., Umili, G., & Vinciguerra, S. (2016). Multiscale geophysical characterization of an unstable rock mass. *Tectonophysics*, *675*, 275–289. https://doi.org/10.1016/j.tecto.2016.02.045

Colombero, C., Baillet, L., Comina, C., Jongmans, D., & Vinciguerra, S. (2017). Characterization of the 3-D fracture setting of an unstable rock mass: From surface and seismic investigations to numerical modeling. *Journal of Geophysical Research: Solid Earth*, *122*, 6346–6366. https://doi.org/10.1002/2017JB014111

Diodati, P., Marchesoni, F., & Piazza, S. (1991). Acoustic emission from volcanic rocks: An example of self-organize criticality. *Physical Review Letters*, *67*(17), 2239–2243. https://doi.org/10.1103/PhysRevLett.67.2239

Eppes, M. C., McFadden, L., Wegmann, K., & Scuderi, L. (2010). Cracks in desert pavement rocks: Further insights into mechanical weathering by directional solar heating. *Geomorphology*, *123*(1-2), 97–108. https://doi.org/10.1016/j.geomorph.2010.07.003

Fazio, M., Benson, P. M., & Vinciguerra, S. (2017). On the generation mechanisms of fluid-driven seismic signals related to volcano-tectonics. *Geophysical Research Letters*, *44*, 734–742. https://doi.org/10.1002/2016GL070919

Gambino, S. P., Mostaccio, A., Patanè, D., Scarfi, L., & Ursino, A. (2004). High-precision locations of the microseismicity preceding the 2002–2003 Mt. Etna eruption. *Geophysical Research Letters*, *31*, L18604. https://doi.org/10.1029/2004GL020499

Garbini, J. (2009). Instrumentation and analysis of the diurnal processes affecting a natural boulder exposed to a natural environment (UNC Charlotte thesis) (148 pp.).

Gariano, S. L., & Guzzetti, F. (2016). Landslides in a changing climate. *Earth-Science Reviews*, *162*, 227–252. https://doi.org/10.1016/j.earscirev.2016.08.011

Girard, L., Gruber, S., Weber, S., & Beutel, J. (2013). Environmental controls of frost cracking revealed through in situ acoustic emission measurements in steep bedrock. *Geophysical Research Letters*, *40*, 1748–1753. https://doi.org/10.1002/grl.50384

Gunzburger, Y., Merrien-Soukatchoff, V., & Guglielmi, Y. (2005). Influence of daily surface temperature fluctuations on rock slope stability: Case study of the Rochers de Valebres slope (France). *International Journal of Rock Mechanics and Mining Sciences*, *42*(3), 331–349. https://doi.org/10.1016/j.ijrmms.2004.11.003

Halsey, D. (1996). The weathering of sandstone, with particular reference to buildings in the west midlands, UK (PhD thesis). University of Wolverhampton.

Hardy, H. R. (2003). *Acoustic emission/microseismic activity—Principles, techniques and geotechnical applications*. Lisse, Netherlands: A. A. Balkema. https://doi.org/10.1201/9780203971109

Helmstetter, A., & Garambois, S. (2010). Seismic monitoring of Séchilienne rockslide (French alps): Analysis of seismic signals and their correlation with rainfalls. *Journal of Geophysical Research*, *115*, F03016. https://doi.org/10.1029/2009JF001532

Lévy, C., Baillet, L., Jongmans, D., Mourot, P., & Hantz, D. (2010). Dynamic response of the Chamousset rock column (western alps, France). *Journal of Geophysical Research*, *115*, F04043. https://doi.org/10.1029/2009JF001606

Lévy, C., Jongmans, D., & Baillet, L. (2011). Analysis of seismic signals recorded on a prone-to-fall rock column (Vercors massif, French Alps). *Geophysical Journal International*, *186*(1), 296–310. https://doi.org/10.1111/j.1365-246X.2011.05046.x

Lockner, D. A., Byerlee, J. D., Kuksenko, V., Ponomarev, A., & Sidorin, A. (1991). Quasi-static fault growth and shear fracture energy in granite. *Nature*, *350*(6313), 39–42. https://doi.org/10.1038/350039a0

Lomax, A., Virieux, J., Volant, P., & Berge, C. (2000). Probabilistic earthquake location in 3D and layered models: Introduction of a metropolis-Gibbs method and comparison with linear locations. In C. H. Thurber & N. Rabinowitz (Eds.), *Advances in Seismic Event Location* (pp. 101–134). Amsterdam: Kluwer. https://doi.org/10.1007/978-94-015-9536-0_5

McFadden, L. D., Eppes, M. C., Gillespie, A. R., & Hallet, B. (2005). Physical weathering in arid landscapes due to diurnal variation in the direction of solar heating. *Geological Society of America Bulletin*, *110*, 161–173.

McKay, C. P., Molaro, J. L., & Marinova, M. M. (2009). High-frequency rock temperature data from hyper-arid desert environments in the Atacama and the Antarctic dry valleys and implications for rock weathering. *Geomorphology*, *110*(3-4), 182–187. https://doi.org/10.1016/j.geomorph.2009.04.005

Molaro, J. L., & McKay, C. P. (2010). Processes controlling rapid temperature variations on rock surfaces. *Earth Surface Processes and Landforms*, *35*, 501–507. https://doi.org/10.1002/esp.1957

Moores, J. E., Pelletier, J. T., & Smith, P. H. (2008). Crack propagation by differential insolation on desert surface clasts. *Geomorphology*, *102*(3-4), 472–481. https://doi.org/10.1016/j.geomorph.2008.05.012

Paranunzio, R., Laio, F., Nigrelli, G., & Chiarle, M. (2015). A method to reveal climatic variables triggering slope failures at high elevation. *Natural Hazards*, *76*(2), 1039–1061. https://doi.org/10.1007/s11069-014-1532-6

Regione, P. (1993). La rete di controllo della rupe di Madonna del Sasso, sintesi dei risultati dei primi 18 mesi di misure. Assessorato Difesa del Suolo e Governo Risorse Idriche. Settore per la prevenzione del rischio geologico, meteorologico e sismico. Servizio interventi progettuali geologico-tecnici, pronto intervento e verifica grandi opere infrastrutturali (Technical Report, 52 pp.).

Sammonds, P. R. (1999). Understanding the fundamental physics governing the evolution and dynamics of the Earth's crust and ice sheets. *Philosophical Transactions. Royal Society of London*, *357*(1763), 3377–3401. https://doi.org/10.1098/rsta.1999.0499

Senfaute, G., Duperret, A., & Lawrence, J. (2009). Micro-seismic precursory cracks prior to rockfall on coastal chalk cliffs: A case study at Mesnil-Val, Normandie, France. *Natural Hazards and Earth System Sciences*, *9*(5), 1625–1641. https://doi.org/10.5194/nhess-9-1625-2009

Spillmann, T., Maurer, H., Green, A. G., Heincke, B., Willenberg, H., & Husen, S. (2007). Microseismic investigation of an unstable mountain slope in the Swiss Alps. *Journal of Geophysical Research*, *112*, B07301. https://doi.org/10.1029/2006JB004723

Swami, S. G. (2011). Temperature, strain and acoustic emission monitoring of a natural boulder exposed to the Sun: A test on the efficacy of insolation on physical weathering (UNC Charlotte thesis) (148 pp.).

Walter, M., & Joswig, M. (2009). *Seismic characterization of slope dynamics caused by soft rock-landslides: The super-Sauze case study, in landslide processes: From geomorphic mapping to dynamic modelling, proceedings of the landslide processes conference* (pp. 215–220). Strasbourg, France: CERG editions.

Warren, K., Eppes, M.-C., Swami, S., Garbini, J., & Putkonen, J. (2013). Automated field detection of rock fracturing, microclimate, and diurnal rock temperature and strain fields. *Geoscientific Instrumentation, Methods and Data Systems*, *2*(2), 275–288. https://doi.org/10.5194/gi-2-275-2013

Yatsu, E. (1988). *The nature of weathering: An introduction* (624 pp.). Tokyo: Sozosha.

Young, R. P., & Collins, D. S. (2001). Seismic studies of rock fracture at the underground research laboratory. *Canada, International Journal of Rock Mechanics & Mining Sciences*, *38*(6), 787–799. https://doi.org/10.1016/S1365-1609(01)00043-0